

Identifying Pediatric Vascular Anomalies With Deep Learning

Justin Chan,¹ Sharat Raju^{2,3}, Randy Bly^{2,3*}, Jonathan A. Perkins^{2,3*} and Shyamnath Gollakota^{1*}

¹Paul G. Allen School of Computer Science and Engineering, University of Washington, WA

²Department of Otolaryngology – Head and Neck Surgery, University of Washington, WA

³Seattle Children's Hospital and Research Institute, Seattle, WA

*Correspondence authors: jonathan.perkins@seattlechildrens.org, randbly@uw.edu, gshyam@uw.edu

Vascular anomalies, more colloquially known as birthmarks, affect up to 1 in 10 infants^{1,2}.

Though many of these lesions self-resolve, some types can result in medical complications or disfigurement without proper diagnosis or management. Unfortunately, vascular anomalies are challenging for pediatricians and primary care physicians to accurately diagnose due to subtle visual differences and similarity to other pediatric dermatologic conditions. This can result in delayed or incorrect referrals for treatment. To address this problem, we developed a convolutional neural network (CNN) to automatically classify images of vascular anomalies and other pediatric skin condition to aid physicians with diagnosis. We constructed a dataset of 21,681 clinical images, including data collected between 2002–2018 at Seattle Children's hospital and five dermatologist-curated online repositories, and built a taxonomy over a set of nine vascular anomalies and six common pediatric skin lesions. The CNN achieved an average AUC of 0.9731 when ten-fold cross-validation was performed across all classes. The classifier's average AUC and weighted F_1 score was 0.9889 and 0.9732 respectively when evaluated on a held-out test

set of six classes. When used as an aid for pediatricians (n = 6), the classifier increased their average visual diagnostic accuracy from 73.67% to 92.00%. The classifier runs real-time on a smartphone and has the potential to improve management of these conditions, particularly in resource-limited areas.

Introduction

Vascular anomalies, colloquially known as “birthmarks”, affect between 5 and 13%^{3,4} of all infants. Most are associated with changes in the appearance of the overlying skin, and initial diagnosis is commonly made by history and physical exam, a large part of which is visual inspection.

Vascular anomalies encompass a large number of diagnoses which are classified by the International Society for the Study of Vascular Anomalies (ISSVA) into vascular tumors and vascular malformations. Some vascular anomalies, such as nevus simplex and certain infantile hemangiomas, will fade with time and can be managed medically or with observation in the primary care setting^{5,6}. In contrast, venous malformations, congenital hemangiomas, and lymphatic malformations are best managed early by a multidisciplinary team of specialists including dermatologists, surgeons, and pediatricians. Without proper treatment, bleeding, infection, permanent disfigurement, or airway complications may occur. As a result, early and correct diagnosis is critical to prevent delays in management^{7,8}.

Accurate diagnosis of vascular anomalies is challenging. They can occur on any surface of the body, and the skin manifestations can include a wide range of sizes and hues. As a result, these lesions can be difficult to visually differentiate, and it has been shown that as low as 31 - 53% of vascular

anomalies have a correct diagnosis at the time of referral^{8–10}. Additionally, some of these anomalies may be confused with common pediatric dermatologic conditions. This can lead to inaccurate expectations from patients and families, and in some cases, delays in delivery of care. Thus, to assist pediatricians and other primary care physicians with accurate diagnosis, we develop an image classification system which uses a convolutional neural network (CNN) to automatically classify images of vascular anomalies.

A computer-aided system for classifying vascular anomalies currently does not exist, partly due to the sparsity of labeled imaging data. At most tertiary vascular anomaly centers, proper diagnosis and staging relies on a combination of modalities including clinical history and exam, imaging, angiography, tissue biopsy, and multidisciplinary consensus^{3,8}. However, these are not readily available in the primary care setting.

In this study, we construct a dataset of 21,681 labeled images of cutaneous skin lesions spanning 15 different pediatric dermatologic conditions including nine vascular anomalies. 10,700 images in the dataset are collected from Seattle Children’s Hospital during 2002–2018 as clinical photographs were routinely obtained for all patients visiting the vascular anomaly clinic. Additionally, we include 10,981 dermatologist-curated images from five open-access online repositories to supplement image classes that were sparse or did not exist in our clinical dataset. We developed a CNN,¹¹ a type of deep learning system optimized for image classification, to visually identify and diagnose vascular anomalies. CNNs are able to automatically learn representations of input data and make predictions without the need for extensive pre-processing and feature engineering¹². CNNs have shown specialist-level accuracy at diagnosing diseases such as melanoma¹³, pneumonia¹⁴, diabetic retinopathy¹⁵ and

cardiovascular risk¹⁶. We demonstrate that such a tool can **improve** diagnostic accuracy **for vascular anomalies and other pediatric dermatologic conditions** among a cohort of pediatricians and primary care physicians.

Results

All images collected from Seattle Children’s **Hospital** were diagnosed by biopsy, computerized tomography (CT), angiography, ultrasonography, or specialist consensus when possible. The images selected for inclusion were further curated by three vascular anomaly surgeons to exclude lesions without cutaneous manifestation. All images were de-identified and manually cropped to only include the area relevant for diagnosis. These images are organized into a taxonomy of 12 different vascular anomaly and pediatric dermatologic classes as shown in Fig. 1a. Vascular anomalies classified under the same taxonomy, such as venous and glomuvenous malformations, were grouped together. Fig. 1b shows example images for each of the 12 classes, illustrating the visual similarity among these lesions.

We use a technique known as transfer learning¹⁷ to classify the images of our dataset. We leverage the InceptionV3 CNN¹⁸ that has been pre-trained on the 2012 ImageNet Large Scale Visual Recognition Challenge (ILSVRC)¹⁹ containing 1000 classes, and then fine tune the weights of the network to our dataset of images. To do this we remove the final softmax layer that produces outputs for the 1000 ImageNet classes. We then add our own layers as shown in Fig. S1 that ends in a softmax output that produces probability outputs for our 12 image classes. We first validate our classifier using 10-fold cross-validation²⁰.

Due to an unequal number of images in each **skin lesion** class, images within the dataset are augmented using label-preserving transformations^{21,22}. We augment each class used for cross-validation to 1000 images. This is to ensure the classifier is not overly biased towards one particular class, or fails to learn a sparse class. This class size was chosen to align with the ImageNet dataset²³, which contains an average of 500–1000 images within each subcategory. Specifically, images are rotated at a random angle and a horizontal and vertical flip are also applied at random. Shear up to an intensity of 0.2 and a zoom in the range 0.8 and 1.2 is applied to the image^{11,13}. Classes that had more than 1000 images were randomly sampled for cross-validation. Images are then resized to 299×299 dimensions to be compatible with the input dimensions of our pre-trained CNN. The data split between the training and validation sets was such that images of the same lesion from multiple angles did not exist in both the training and validation set for any fold. This ensures that the CNN does not leverage patient-specific information when making a prediction. The cross-validation results in Table 1 show the AUCs, confidence intervals and F_1 score for each of the 12 classes. To calculate the F_1 score, the probability threshold for each class is set to maximize the sum of the sensitivity and specificity on that class’ ROC curve. The F_1 score is then weighted in accordance to the number of positive and negative examples of that class. The average AUC and F_1 score across all classes is 0.9731 and 0.9367 respectively.

Next, we evaluate the test performance of our classifier on a held-out independent dataset. Due to the sparsity of images of lymphatic malformations and spider angiomas, meaningful performance values cannot be generated for those classes. The criteria for a sufficient number of images in a test class is based on the composition of images in the ILSVRC which has 50–100 images per test class.

To obtain meaningful test performance values, we selected six classes that were sufficiently data abundant and most commonly seen in practice based on consensus by vascular anomaly specialists and dermatologists (Fig. 1a). For classes with more than 1000 images, images not sampled for cross-validation are used in the test set. For the remaining classes, 10% of the total number of images in that class were withheld from the prior cross-validation step, and included in the test set. The cross-validation results over these six classes are shown in Supplementary Table 1, the average AUC and F_1 score across six classes is 0.98384 and 0.9485 respectively. We show the individual receiver-operating characteristic (ROC) curves for the classifier’s test performance on each of these six classes in Fig. 3.

The average AUC across these six classes is 0.9889. and the average weighted F_1 score is 0.9732

Table S2.

We generate saliency maps in Fig. S2 for an example image in each class of our 12-class taxonomy using integrated gradients²⁴. The maps confirm that the CNN places more weight on the pixels representing the lesion compared to surrounding skin when making a prediction. Additionally, we visualize the features learned at the last layer of our CNN classifier using t-SNE for our 6-class taxonomy in Fig. S3. The projection of features onto a 2-D space shows that each class is clustered tightly and are separated from the clusters of other classes.

We next evaluate if our CNN trained on six lesion classes can be used to aid pediatricians to more accurately diagnose vascular anomalies, and thus make appropriate referrals. We presented 60 images from our test set to six pediatricians. Only clear and visible images were selected for inclusion in this subset. On this subset of 60 test images, our classifier had an accuracy of 93.33%. Each pediatrician was asked to classify each image into one of six classes. Pediatricians achieved

an average accuracy of 73.67% on this task. The pediatricians were not informed of their accuracy or of the ground truth of the images during their initial pass. They were then presented with the same set of images in a different order, each annotated with the classifier's predictions, and asked to classify each image. When aided with the classifier's predictions, the average accuracy increased to 92.00%. We compare the confusion matrix across all pediatricians when they are unaided and aided with our classifier (Fig. 3) The figure shows that pediatrician accuracy is increased across all six classes. Additionally, when aided with the classifier, pediatricians are able to achieve higher accuracies for venous malformations and atopic dermatitis than when using the classifier alone. This suggests that combining the computer-aided system with pediatrician expertise has an advantage over either method alone.

Finally, we evaluate if our classifier can be deployed and executed on a smartphone in real-time (Fig. S4). On an iPhone 7, the classifier makes real-time predictions within 32 ms, and can be readily deployed for use in clinical settings.

Discussion

Early and accurate diagnosis of vascular anomalies is essential to minimize complications and ensure appropriate treatment. For many primary care physicians, diagnosis relies on identifying subtle visual clues. We present data that a CNN trained on images of vascular anomalies and other common pediatric skin lesions can enhance the diagnostic accuracy of physicians, which may improve outcomes and optimize referral patterns.

A limitation of our dataset is the imbalance of images across different classes. This is reflected

in the increased prevalence of certain vascular anomalies such as **infantile hemangiomas**. As a result the number of images available in the test set for evaluation are relatively small for pyogenic granulomas (**lobular hemangioma**) and venous malformations. Acquiring images of more sparse diagnostic classes would allow us to more accurately estimate the real world performance of the classifier on these lesion types. We note however that a clinical deployment of this system may benefit from intentionally biasing the classifier to incorporate real world prevalence rates of different vascular anomalies when making a prediction. Evaluating the classifier in a **larger** prospectively obtained cohort may provide a more robust estimate of accuracy and potential clinical impact. Additionally, though the CNN can be deployed on a commodity smartphone, variations in the quality and setting of the photos may affect real-world classification accuracy. In particular, evaluating the classifier on images taken with multiple smartphone cameras would be needed to test how well our classifier generalizes to images obtained in primary care clinical settings. Also, developing a CNN to identify the location of a lesion in an uncropped image and to tolerate nonideal lighting conditions could be useful in some clinical scenarios. Finally, diagnosis of vascular anomaly lesions is multifactorial and requires a history, exam, palpation, imaging (ultrasonography, CT, MRI), and biopsy in some cases. Though visual inspection is one of the most important diagnostic tools, the overall context is needed to make a clinical decision.

Given the prevalence of vascular anomalies, computer-aided diagnosis has the potential to improve health care outcomes and reduce the cost associated with delayed or incorrect referrals. It may also have particular benefit in resource-limited regions, where tertiary expertise is unavailable but smartphones are increasingly ubiquitous. For future studies, we envision that computer-aided diag-

nosis of vascular anomalies could not only augment the capabilities of primary care physicians, but also guide specialists in treatment of these conditions. For example, a similar classifier could inform clinicians about outcomes related to infantile hemangioma and predict response to propranolol treatment.

Methods

Datasets. This study was approved by the Seattle Children’s Institutional Review Board. All data was de-identified in accordance with HIPAA guidelines. Our dataset is composed of clinical data from Seattle Children’s from 2002-2018, as well as the open-access dermatology repositories, DermIS²⁵, DermNet²⁶, DermNetNZ²⁷, DermQuest²⁸ and the ISIC dermoscopic archive²⁹. The images from Seattle Children’s consist of hemangiomas (infantile and congenital), pyogenic granuloma (**lobular hemangioma**), venous and glomuvenous malformations, capillary malformations, Sturge-Weber syndrome, spider angioma and lymphatic malformations. The images from the open-access repositories consist of pyogenic granuloma, atopic dermatitis, nevus, spider angioma, milia, lymphatic malformations, impetigo, molluscum and tinea.

Training algorithm. To train our dataset, we first removed the final 1000-node softmax layer of the InceptionV3 neural network, we then fine-tune the classifier with our own layers (Fig. S1) using the Keras framework. We add a 256-node fully-connected layer, with a ReLu activation, followed by Dropout regularization with a rate of 0.6, and finally a 6-way or 12-way softmax layer, depending on the taxonomy of vascular anomalies being classified. We used the RMSProp optimizer with a learning rate of $1e^{-5}$ and a rho value of 0.9. We used the sklearn library for calculating performance measures

including AUC and F_1 score.

t-SNE algorithm. The t-SNE plot was generated using an implementation of Barnes-Hut t-SNE^{30,31} using a perplexity value of five, the algorithm was run for 1,000 iterations.

Saliency maps. The saliency maps were generated with an implementation of integrated gradients^{24,32}. The output is smoothed using the SmoothGrad³³ algorithm to produce a sharper map.

Run-time analysis. We timed an implementation of the CNN running in real-time on an iPhone 7. The CNN was ported to the iOS platform using Apple's Core ML tools library which converts the CNN to an iPhone readable format.

Data availability statement. All data necessary for interpreting the manuscript have been included. The datasets used in the current study are not publicly available but may be available from the corresponding authors on reasonable request and with permission of Seattle Children's hospital and the University of Washington. Images from the online repositories are publicly available at DermIS²⁵, DermNet²⁶, DermNetNZ²⁷, DermQuest²⁸ and the ISIC dermoscopic archive²⁹.

Use of human subjects. All human subjects were practicing pediatricians and took our tests under informed consent. This study was approved as exempt by the Seattle Children's Institutional Review Board.

Supplementary Materials

Fig. S1. Convolutional neural network architecture.

Fig. S2. Saliency maps for each for 12 pediatric skin lesion classes

Fig. S3. t-SNE visualization of the CNN's weights.

Fig. S4. User interface of CNN running on a smartphone.

Table S1. Cross-validation performance over six classes

Table S2. F_1 score on test set of six classes.

Acknowledgments. The authors thank Jacob Sunshine, and John Thickstun for feedback on the manuscript. The authors also thank Allegro Pediatrics–Issaquah Highlands Group for participation and Eden Palmer for photography and vascular anomaly photographic archive.

Author contributions. SR conceptualized the study; JC designed the algorithms and conducted the analysis with technical supervision by SG; JC, SR and SG wrote the manuscript; RB and JP edited the manuscript; RB and JP recruited the pediatricians for the study; JP provided the data used in the analysis.

Competing interest statement. JC, SR, RB and SG have equity stakes in Edus Health, Inc., which is not related to the technology presented in this manuscript. SG is a co-founder of Jeeva Wireless, Inc. and Sound Life Sciences, Inc. RB is a consultant for SpiWay, LLC and a co-founder of EigenHealth, Inc.

References

1. Vascular anomalies (2019). URL <https://www.chop.edu/conditions-diseases/vascular-anomalies>.
2. Vascular anomalies (2019). URL <https://www.uchicagomedicine.org/comer/conditions-services/vascular-anomalies>.
3. Nosher, J. L., Murillo, P. G., Liszewski, M., Gendel, V. & Gribbin, C. E. Vascular anomalies: a pictorial review of nomenclature, diagnosis and treatment. *World journal of radiology* **6**, 677 (2014).

4. Greene, A. K. *et al.* Risk of vascular anomalies with down syndrome. *Pediatrics* **121**, e135–e140 (2008).
5. Juern, A. M., Glick, Z. R., Drolet, B. A. & Frieden, I. J. Nevus simplex: a reconsideration of nomenclature, sites of involvement, and disease associations. *Journal of the American Academy of Dermatology* **63**, 805–814 (2010).
6. Haggstrom, A. N. *et al.* Prospective study of infantile hemangiomas: clinical characteristics predicting complications and treatment. *Pediatrics* **118**, 882–887 (2006).
7. Lee, J. W. & Chung, H. Y. Vascular anomalies of the head and neck: current overview. *Archives of craniofacial surgery* **19**, 243 (2018).
8. Greene, A. K., Liu, A. S., Mulliken, J. B., Chalache, K. & Fishman, S. J. Vascular anomalies in 5621 patients: guidelines for referral. *Journal of pediatric surgery* **46**, 1784–1789 (2011).
9. Levin, D. E. *et al.* Room for improvement: Patterns of referral misdiagnosis to a vascular anomalies center. *Open Journal of Pediatrics* **3**, 331 (2013).
10. MacFie, C. C. & Jeffery, S. L. Diagnosis of vascular skin lesions in children: an audit and review. *Pediatric dermatology* **25**, 7–12 (2008).
11. Krizhevsky, A., Sutskever, I. & Hinton, G. E. Imagenet classification with deep convolutional neural networks. In *Advances in neural information processing systems*, 1097–1105 (2012).

12. Nixon, M. & Aguado, A. S. *Feature extraction and image processing for computer vision* (Academic Press, 2012).
13. Esteva, A. *et al.* Dermatologist-level classification of skin cancer with deep neural networks. *Nature* **542**, 115 (2017).
14. Rajpurkar, P. *et al.* Chexnet: Radiologist-level pneumonia detection on chest x-rays with deep learning. *arXiv preprint arXiv:1711.05225* (2017).
15. Gulshan, V. *et al.* Development and validation of a deep learning algorithm for detection of diabetic retinopathy in retinal fundus photographs. *Jama* **316**, 2402–2410 (2016).
16. Poplin, R. *et al.* Prediction of cardiovascular risk factors from retinal fundus photographs via deep learning. *Nature Biomedical Engineering* **2**, 158 (2018).
17. Pan, S. J. & Yang, Q. A survey on transfer learning. *IEEE Transactions on knowledge and data engineering* **22**, 1345–1359 (2010).
18. Szegedy, C., Vanhoucke, V., Ioffe, S., Shlens, J. & Wojna, Z. Rethinking the inception architecture for computer vision. In *Proceedings of the IEEE conference on computer vision and pattern recognition*, 2818–2826 (2016).
19. Russakovsky, O. *et al.* Imagenet large scale visual recognition challenge. *International journal of computer vision* **115**, 211–252 (2015).

20. Kohavi, R. *et al.* A study of cross-validation and bootstrap for accuracy estimation and model selection. In *Ijcai*, vol. 14, 1137–1145 (Montreal, Canada, 1995).
21. Cireşan, D., Meier, U. & Schmidhuber, J. Multi-column deep neural networks for image classification. *arXiv preprint arXiv:1202.2745* (2012).
22. Simard, P. Y., Steinkraus, D., Platt, J. C. *et al.* Best practices for convolutional neural networks applied to visual document analysis.
23. Deng, J. *et al.* Imagenet: A large-scale hierarchical image database. In *2009 IEEE conference on computer vision and pattern recognition*, 248–255 (Ieee, 2009).
24. Sundararajan, M., Taly, A. & Yan, Q. Axiomatic attribution for deep networks. In *Proceedings of the 34th International Conference on Machine Learning-Volume 70*, 3319–3328 (JMLR. org, 2017).
25. Dermis.net (2019). URL <https://www.dermis.net/dermisroot/en/home/index.htm>.
26. Dermnet (2019). URL www.dermnet.com/.
27. Dermnet NZ (2019). URL <https://www.dermnetnz.org/>.
28. DermIS.net (2019). URL <https://www.dermis.net/dermisroot/en/home/index.htm>.
29. ISIC (2019). URL <https://www.isic-archive.com>.
30. Van Der Maaten, L. Barnes-Hut-SNE. *arXiv preprint arXiv:1301.3342* (2013).

31. Python-TSNE (2019). URL <https://github.com/danielfrg/tsne>.
32. deep-viz-keras (2019). URL <https://github.com/experiencor/deep-viz-keras>.
33. Smilkov, D., Thorat, N., Kim, B., Viégas, F. & Wattenberg, M. Smoothgrad: removing noise by adding noise. *arXiv preprint arXiv:1706.03825* (2017).

a.

Class	Lesion type	Vascular anomaly?	Number of images		
			Clinical dataset	Online repositories	Total
1	Infantile hemangioma	✓	9049 + 142 = 9191	0	9191
	Congenital hemangioma				
2	Pyogenic granuloma	✓	95	130	225
3	Venous malformation	✓	365 + 37 = 402	0	402
	Glomuvenuous malformation				
4	Capillary malformation	✓	828 + 40 = 868	0	868
	Sturge Weber				
5	Atopic dermatitis	✗	0	717	717
6	Nevus	✗	0	9307	9307
7	Spider angioma	✓	55	43	98
8	Milia	✗	0	84	84
9	Lymphatic malformation	✓	74	0	74
10	Impetigo	✗	0	91	91
11	Molluscum	✗	0	171	171
12	Tinea	✗	0	438	438
Total			10,685	10,981	21,681

b.

Figure 1: Pediatric skin lesions taxonomy and example images. a. Taxonomy of 12 pediatric skin lesions. The table shows the composition of images which were obtained from the Seattle Children's clinical dataset and dermatologist-curated online repositories. The upper half of the table represents a 6-class subset of our taxonomy where images in each class are comparatively data abundant and consist of pediatric skin lesions more commonly seen in practice. **b.** Example images of the lesions in the 6-class subset of our taxonomy. The images demonstrate the visual similarity between different lesion types.

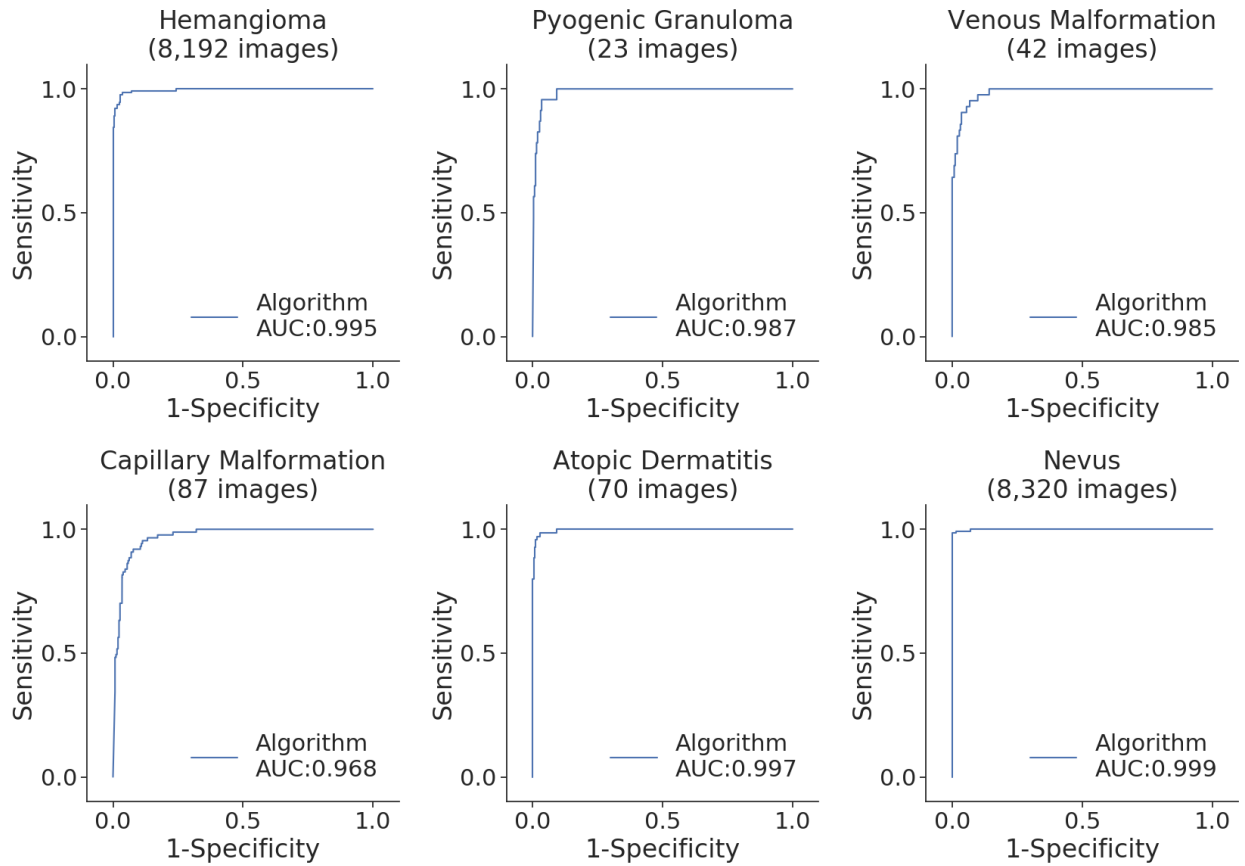


Figure 2: **Classifier performance on a held-out test set.** The receiver-operating curves show the performance of our classifier on a held-out test set of images from our 6-class taxonomy.

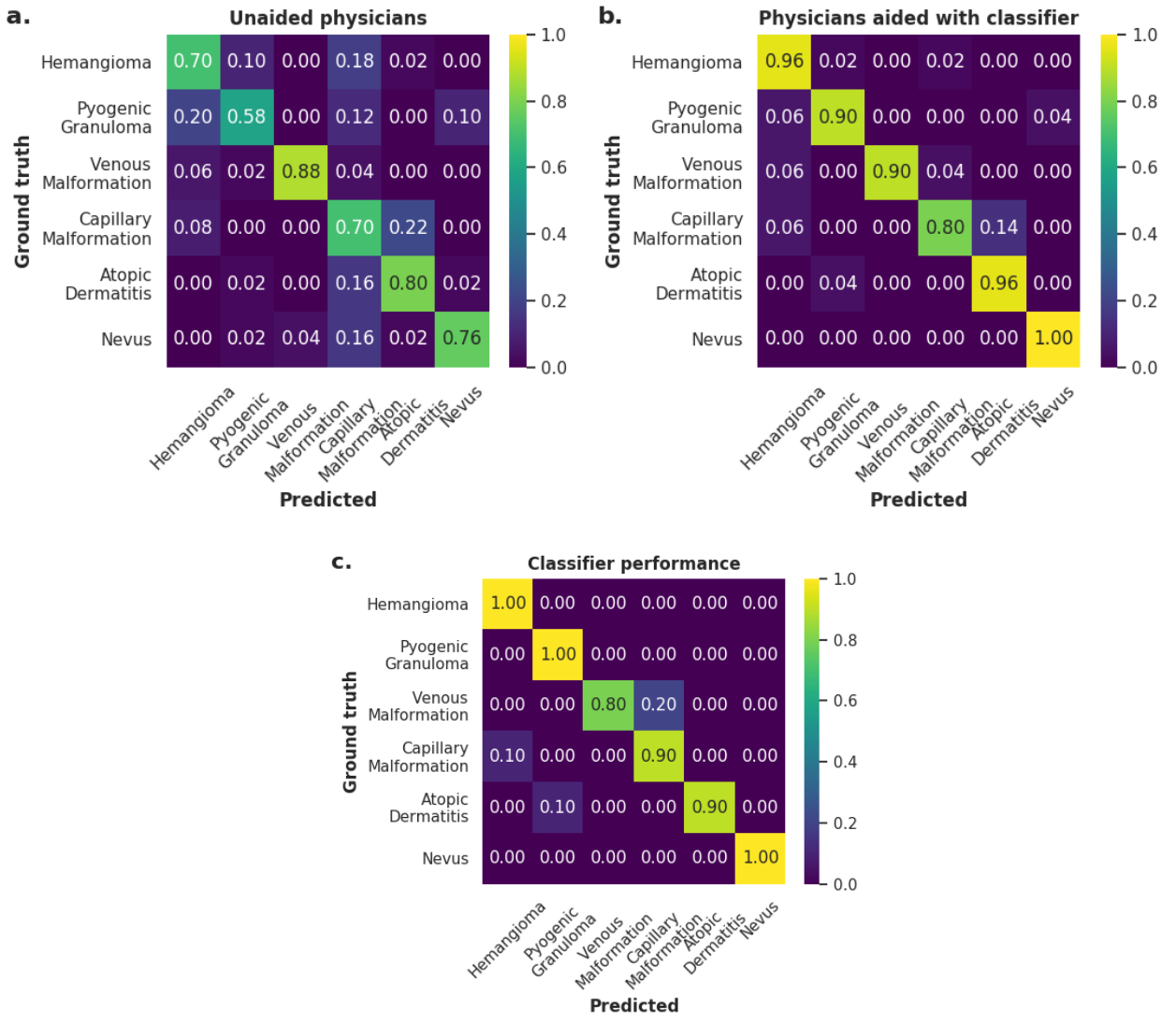
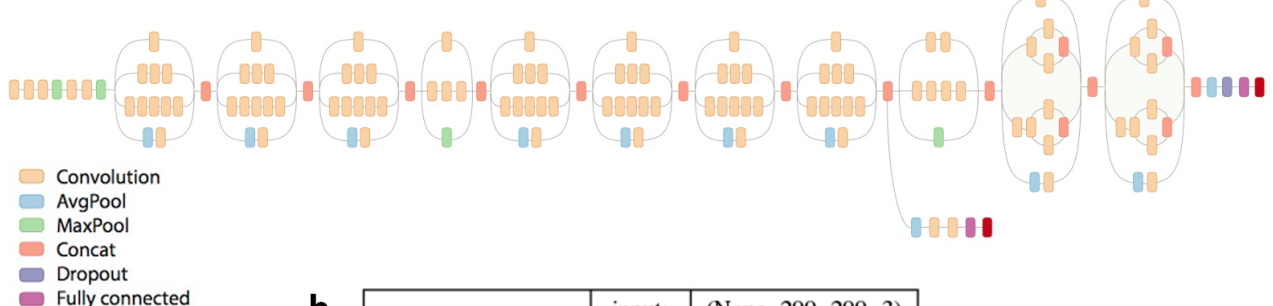


Figure 3: Diagnostic performance of pediatricians without and with the aid of the classifier. The confusion matrices show the diagnostic accuracies of six physicians in a survey containing 60 images drawn uniformly from six pediatric skin lesions. The figure shows the performance **a.** without and **b.** with the aid of our classifier and **c.** the performance of the classifier itself. With the aid of the classifier, diagnostic accuracies are higher for each of the six classes. When aided with the classifier, the physicians achieve higher accuracies for venous malformations and atopic dermatitis compared to the classifier performance alone.

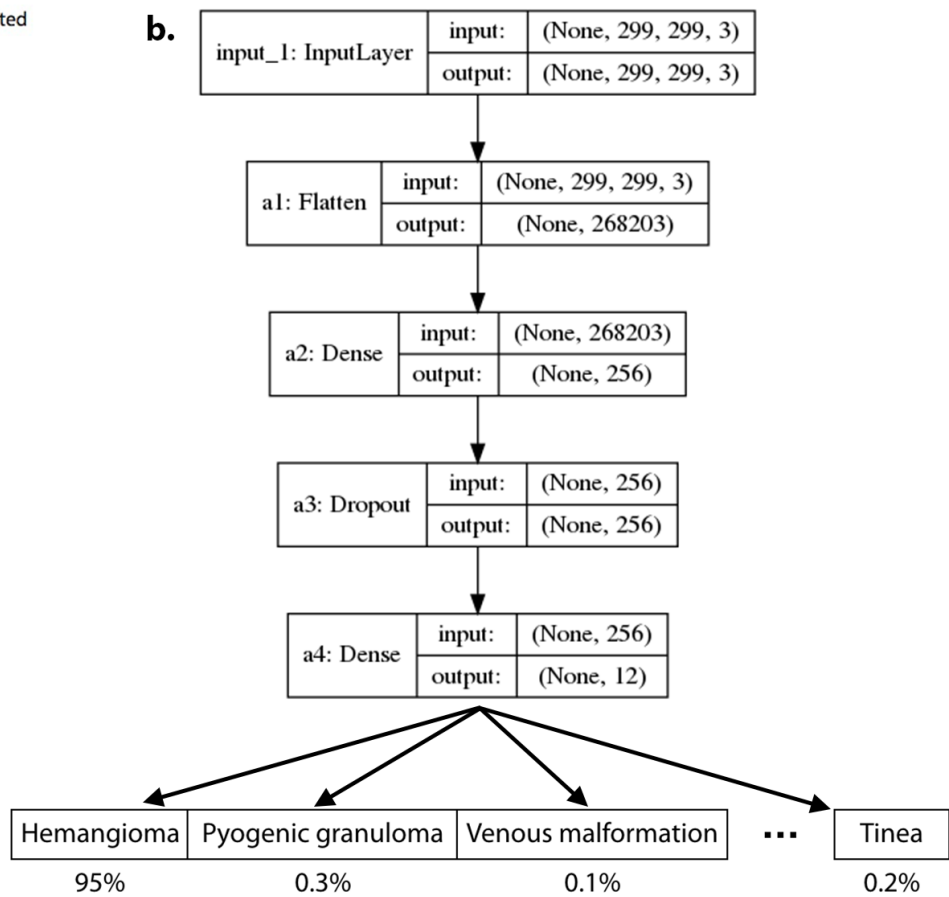
Lesion type	AUC (95% CI)	F_1 score
Hemangioma	0.9608 (0.9514 – 0.9701)	0.9188 (0.8988 – 0.9388)
Pyogenic granuloma	0.9875 (0.9735 – 1.0015)	0.9696 (0.9571 – 0.9822)
Venous+telangiectatic malformation	0.9750 (0.9684 – 0.9816)	0.9374 (0.9237 – 0.9511)
Capillary malformation+Sturge Weber	0.9762 (0.9714 – 0.9810)	0.9373 (0.9228 – 0.9519)
Atopic dermatitis	0.9558 (0.9481 – 0.9634)	0.8996 (0.8783 – 0.9210)
Nevus	0.9994 (0.9990 – 0.9998)	0.9894 (0.9850 – 0.9938)
Spider angioma	0.9716 (0.9603 – 0.9829)	0.9354 (0.9165 – 0.9543)
Lymphatic malformation	0.9279 (0.8957 – 0.9602)	0.8899 (0.8668 – 0.9129)
Milia	0.9967 (0.9957 – 0.9977)	0.9751 (0.9688 – 0.9815)
Impetigo	0.9825 (0.9797 – 0.9853)	0.9372 (0.9298 – 0.9446)
Molluscum	0.9863 (0.9845 – 0.9881)	0.9524 (0.9429 – 0.9619)
Tinea	0.9573 (0.9498 – 0.9648)	0.8984 (0.8875 – 0.9093)
Average	0.9731	0.9367

Table 1: **Cross-validation performance of classifier over 12 classes.** The table shows the AUC and weighted F_1 score of the classifier for each class after performing 10-fold cross-validation over the full taxonomy of 12 lesion types. Additionally, we show the averaged AUC and F_1 score.

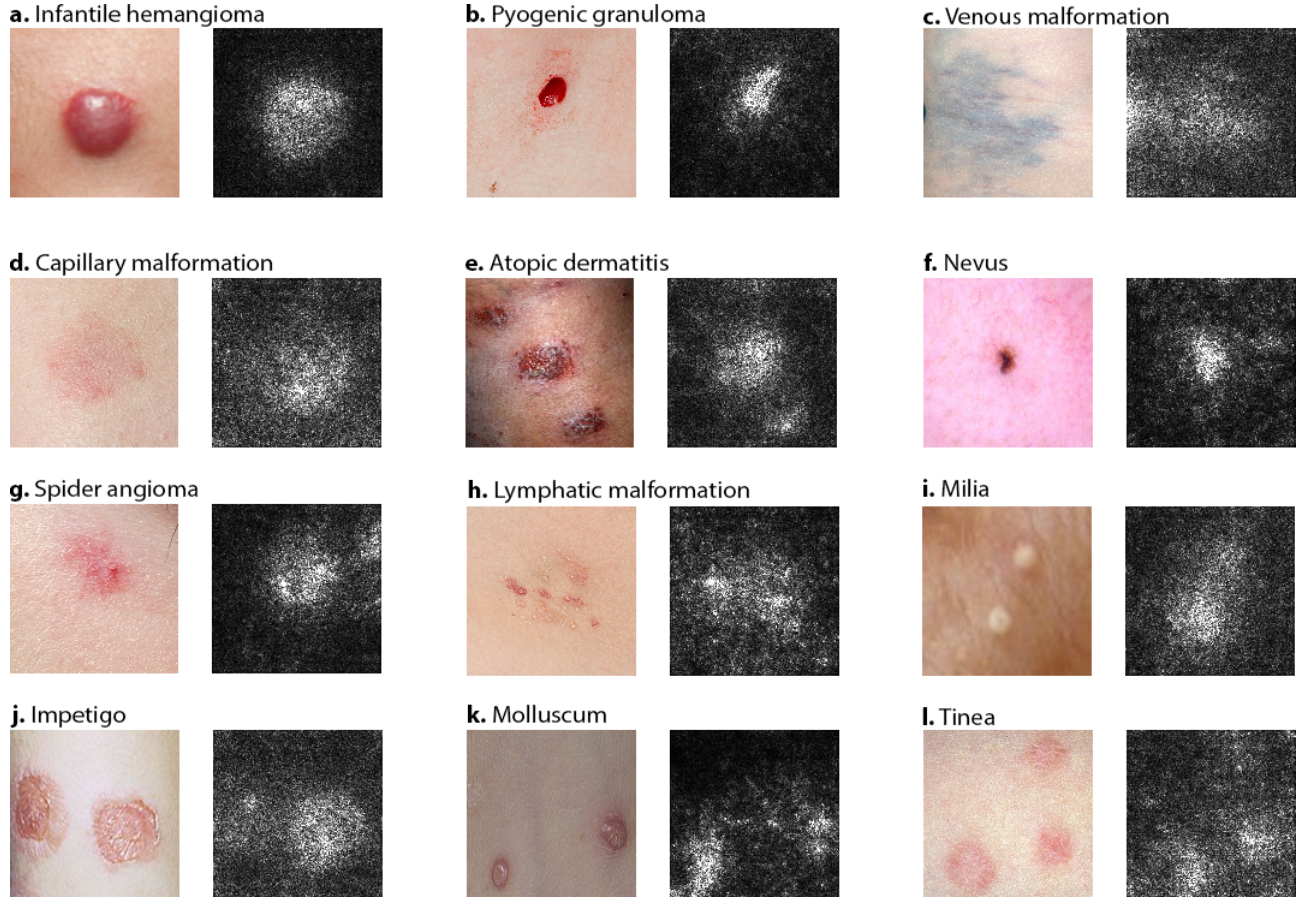
a.



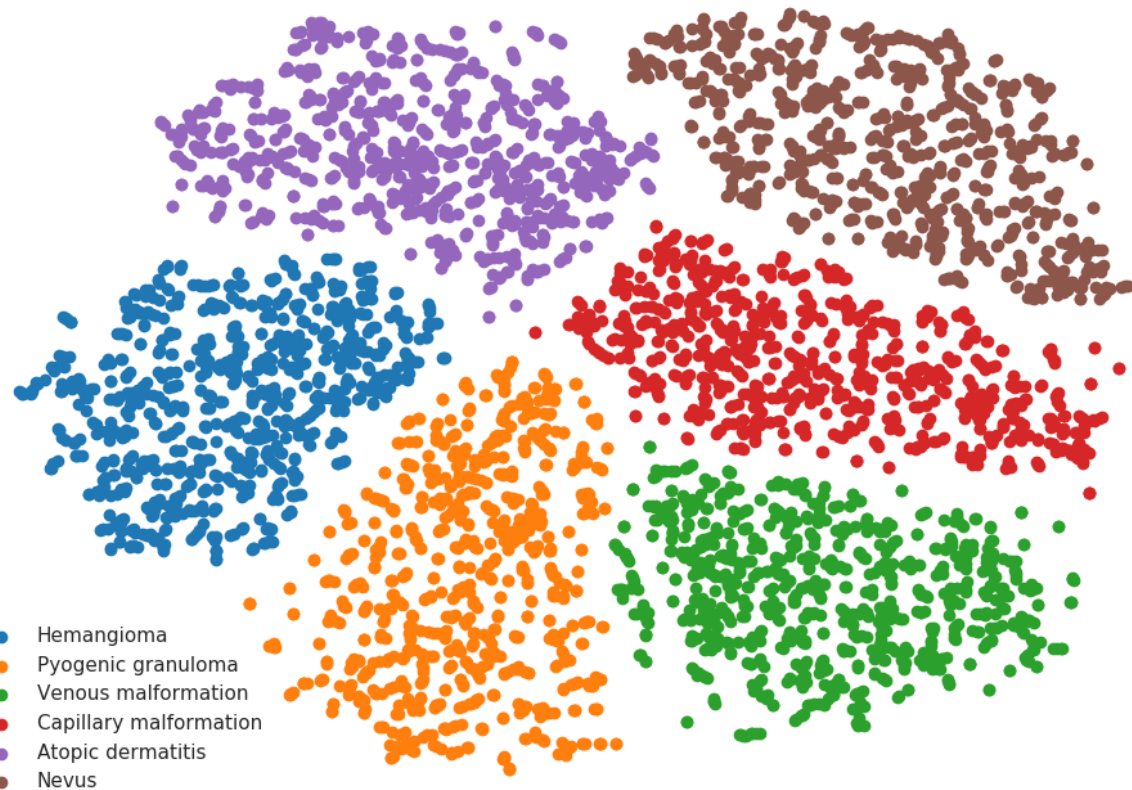
b.



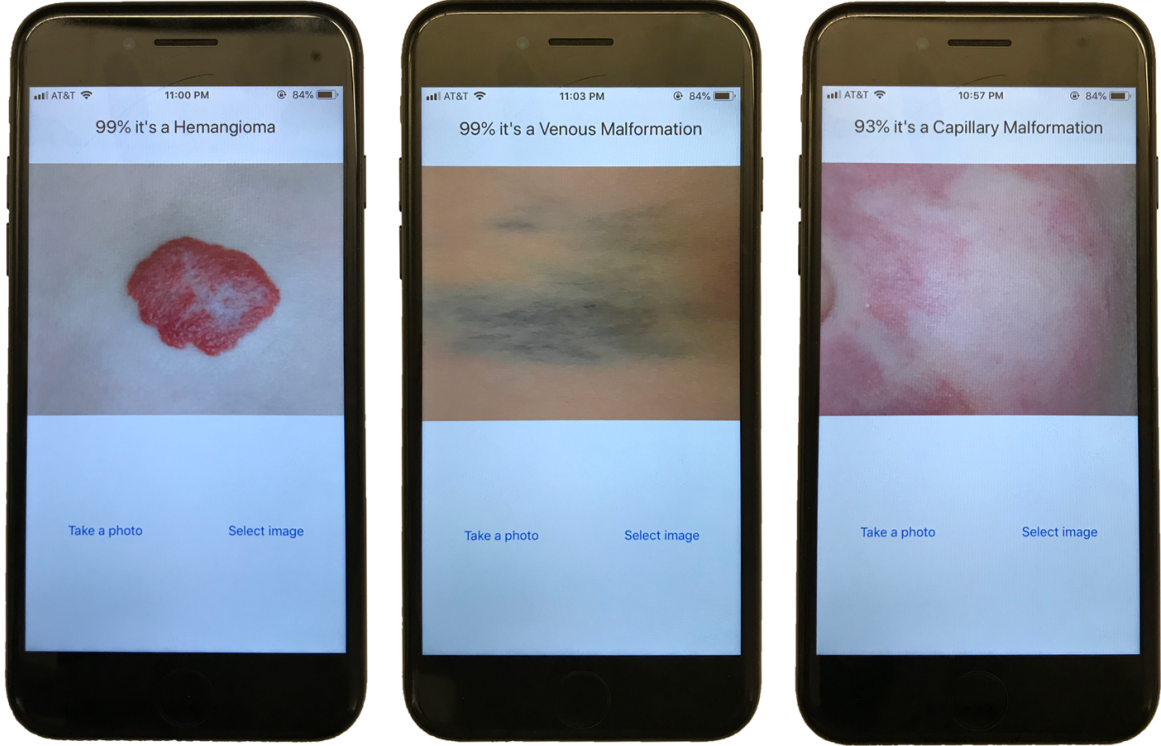
Supplementary Figure 1: **Convolutional neural network architecture.** **a.** We leverage the InceptionV3 network architecture that has been pretrained on the ImageNet dataset. **b.** The weights of the network are fine-tuned on a fully-connected layer of 256 nodes, and outputs a vector of probabilities indicating prediction likelihood for each of the 12 pediatric skin lesion classes.



Supplementary Figure 2: Saliency maps for 12 pediatric skin lesion classes. The saliency maps show which pixels within the image contribute most to the classifier's predictions. White pixels show a greater contribution to the prediction. Each image shows either one or more distinct lesions. The corresponding saliency maps show a correlation between the location of the lesion and the pixels used by the classifier to come to a prediction. **a.** Infantile hemangioma **b.** Pyogenic granuloma **c.** Venous malformation **d.** Capillary malformation **e.** Atopic dermatitis (image from <http://dermquest.com>) **f.** Nevus (source image: <https://www.isic-archive.com>. Image: ISIC_0029072) **g.** Spider angioma **h.** Lymphatic malformation **i.** Milia (source image: https://www.dermnetnz.org/assets/Uploads/lesions/_resampled/ProtectW10/FitWzY0NSw0ODVd/WatermarkedWyIzNDcyMCJd/milia02.jpg) **j.** Impetigo (source image: <http://www.dermnet.com/images/Impetigo/picture/7554>) **k.** Molluscum (source image: <http://www.dermnet.com/images/Molluscum-Contagiosum/picture/9389>) **l.** Tinea (source image: <https://www.dermis.net/dermisroot/en/15811/image.htm>)



Supplementary Figure 3: **t-SNE visualization of the CNN's weights.** The visualization is a projection of the 256 features learned at the final layer of our CNN after it is fine-tuned on our dataset of pediatric skin lesions. The visualization is of a random subset of 5,381 images used to train our CNN.



Supplementary Figure 4: **User interface of CNN running on a smartphone.** The interface allows users to either take a photo or upload an existing image of a pediatric skin lesion. The photo is then passed to our CNN which is running in real time on an iPhone 7. The user is presented with the classifier's prediction and probability output. We show an example of a hemangioma, venous malformation and capillary malformation being classified by our CNN.

Lesion type	AUC (95% CI)	F_1 score
Hemangioma	0.9621 (0.9546 – 0.9696)	0.9084 (0.8943 – 0.9224)
Pyogenic granuloma	0.9933 (0.9891 – 0.9974)	0.9677 (0.9519 – 0.9835)
Venous+telangiectatic malformation	0.9803 (0.9749 – 0.9858)	0.9333 (0.9222 – 0.9444)
Capillary malformation+Sturge Weber	0.9729 (0.9646 – 0.9812)	0.9232 (0.9099 – 0.9364)
Atopic dermatitis	0.9947 (0.9929 – 0.9964)	0.9666 (0.9589 – 0.9743)
Nevus	0.9997 (0.9996 – 0.9999)	0.9916 (0.9891 – 0.9942)
Average	0.98384	0.9485

Supplementary Table 1: **Cross-validation performance over six classes.** The table shows the AUC and weighted F_1 score obtained for each class when performing 10-fold cross-validation over the 6-class subset of our taxonomy. The table also shows the average AUC and F_1 score.

Lesion type	F_1 score
Hemangioma	0.9700
Pyogenic granuloma	0.9810
Venous+gelomuvenous malformation	0.9627
Capillary malformation+Sturge Weber	0.9548
Atopic dermatitis	0.9824
Nevus	0.9883
Average	0.9732

Supplementary Table 2: **F_1 score on test set of six classes.** The table shows the weighted F_1 score when the classifier is evaluated on the test set of six classes. The probability threshold is set to maximize the sensitivity and specificity of that particular class.